LBL-16554

Lawrence Berkeley Laboratory
UNIVERSITY OF CALIFORNIA

Accelerator & Fusion
Research Division

LBL--16554

DE84 003044

Presented at the Third National Conference on Synchrotron Radiation Instrumentation, Brookhaven National Laboratory, Upton, NY, September 12-14, 1983

# THERMAL PROBLEMS ON HIGH FLUX BEAM LINES

R.T. Avery

September 1983

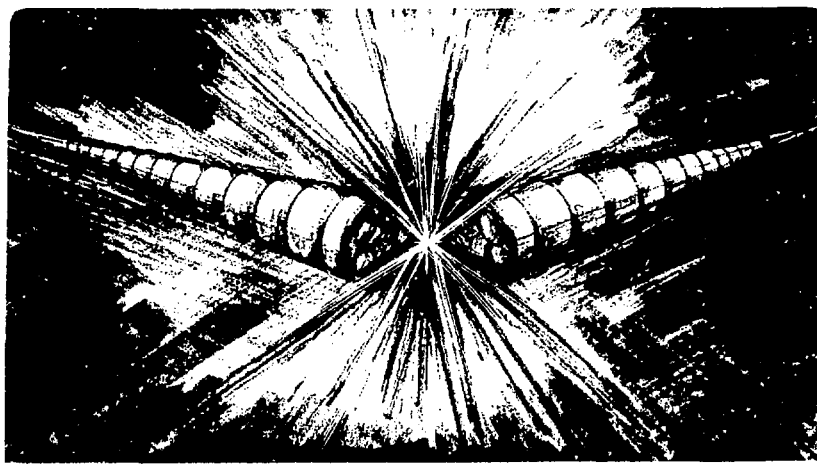

Prepared for the U.S. Department of Energy under Contract DE-AC03-76SF00098

To be presented at the Third
National Conference on Synchrotron
Radiation Instrumentation,
Brookhaven National Laboratory,
Upton, NY, 12-14 September 1983.

LBL-16554

# THERMAL PROBLEMS ON HIGH FLUX BEAM LINES*

Robert T. Avery
Lawrence Berkeley Laboratory
University of California
Berkeley, California 94720

## Abstract

Wiggler and undulator magnets can provide very intense photon flux densities to beam line components. This paper addresses some thermal/materials consequences due to such impingement.

The LBL/Exxon/SSRL hybrid-wiggler Beam Line VI[1] now nearing operation will be able to provide up to ∿ 7 kW of total photon power at planned SPEAR operating conditions. The first masks are located at 6.5 meters from the source and may receive a peak power density (transverse to the beam) exceeding 20 kW/cm$^2$. Significantly, this heat transfer rate exceeds that radiated from the sun's surface (7 kW/cm$^2$) and is comparable to that of welding torches. Clearly, cooling and configuration are of critical importance. Configurations for the first fixed mask, the movable mask, and the pivot mask on this beam line are presented together with considerations of thermal stress fatigue and of heat transfer by conduction to water-cooling circuits. Some preliminary information on heating of crystals and mirrors is also presented.

For the future, many additional intense wiggler/undulator beam lines are contemplated at several storage rings. The design of these beamlines would be enhanced by faster and more accurate computational techniques. LBL is developing a computer code which will be capable of giving photon power densities onto impinged surfaces for a wide range of source and beam line parameters. These include electron beam energy, current, emittance and orbit deviations; wiggler/undulator length, period and magnetic field; photon energy and angular distribution; reflection/absorption at intermediate impinged surfaces; defining apertures and focusing by mirrors. Three-dimensional computer programs for temperature, stress and strain have been available for some years but "user friendly" versions are being sought. Other items to pursue are also suggested.

*This work was supported by the Director, Office of Energy Research, Office of High Energy and Nuclear Physics, Nuclear Science Division, U.S. Department of Energy under Contract Number DE-AC03-76SF00098.

## 1. Introduction

This paper addresses some of the thermal and material problems associated with intense synchrotron radiation from wiggler/undulator magnets striking downstream components. It particularly addresses such effects on the LBL/Exxon/SSRL Beam Line VI now nearing operation.

Synchrotron radiation power levels to be encountered on new wiggler/undulator beamlines generally are much greater than for bend-magnet beam lines. An exception is the high power densities encountered at the "crotch" of bend-magnet ports, solutions for which have been previously described [2,3] and which will not be considered further here.

The construction configurations and analytical methods described herein should be viewed as progress and not as ultimate best solutions. Time and money restrictions have not permitted more sophisticated analysis nor investigation of further alternative methods of construction. Nevertheless, it appears that the Beam Line VI components discussed herein should fully satisfy their design criteria.

## 2. Wiggler/Undulator Photon Power Intensities

The total synchrotron radiation power emanating from a wiggler/undulator magnet has been given by Brown, Halbach, Harris and Winick [4] in practical units as

$$P[W] = 1.27\ E^2\ [GeV^2] \langle B^2\ [T^2] \rangle L[m]\ I\ [A] \qquad (1)$$

with the average taken over the length L. For an N-pole device, the peak power along the scanned direction integrated over the full range of vertical opening angles was given as

$$P'\ [W/mrad] = 4.33\ B_{max}[T]\ E^3\ [GeV^3]\ I\ [A]\ N \qquad (2)$$

The characteristic vertical opening angle of the synchrotron radiation is

$$\Theta_v = \gamma^{-1} \tag{3}$$

and in practical units is

$$\Theta_v \text{ [mrad]} = 0.511 \text{ (E[GeV])}^{-1} \tag{3a}$$

The peak synchrotron radiation power per unit solid angle for sinusoidal magnetic field can be expressed[5] as

$$P'' \text{ [W/(mrad)}^2\text{]} = \frac{1.654\ P}{2\Theta_h \cdot 2\Theta_v} = \frac{1.654\ P}{4K\ \Theta_v^2} \tag{4}$$

where $K = 0.0934\ B_{max}$ [T] $\lambda_w$ [mm] which leads in practical units to

$$P''\text{[W/(mrad)}^2\text{]} = 5.38\ E^4 \text{ [GeV}^4\text{]}\ B_{max} \text{ [T] I [A] N} \tag{4a}$$

For impingement on a surface at a distance z in meters from the mid-length of the wiggler/undulator source, the peak lineal power density and the peak surface power density are

$$W' = \frac{P'}{z} \sin\alpha \tag{5a}$$

$$W'' = \frac{P''}{z^2} \sin\beta \tag{5b}$$

which in practical units become

$$W' \text{ [W/mm]} = P' \text{ [W/mrad] } \sin\alpha \ / \ z \text{ [m]} \tag{5c}$$

$$W'' \text{ [W/mm}^2\text{]} = P'' \text{ [W/(mrad)}^2\text{] } \sin\beta \ / \ z^2 \text{ [m}^2\text{]} \tag{5d}$$

where $\alpha$ is the angle from impinged surface to photon ray measured in the scanning plane and $\beta$ is a similar angle but measured in a plane normal to the surface.

The foregoing power densities in equations (2) through (5d) are based on a negligibly small electron beam size and divergence.

## 2.1 Intensities for LBL/Exxon/SSRL Beam Line VI

The LBL/Exxon/SSRL hybrid-wiggler Beam Line VI is shown in plan view in Figure 1 with the VUV and Soft X-ray branch lines omitted for clarity. Some features of this beam line have been described previously[1].

The SPEAR electron ring and the Beam Line VI hybrid-wiggler magnet can operate in many different modes, three of which are shown in Table I. Mode A represents conditions that might be typical for the first year of Beam Line VI operation. Mode C and E will be achieved in the future when SPEAR is upgraded to deliver beam energies and currents as indicated and with the wiggler magnet gap closed down to permit a peak magnetic field of 1.75 Tesla. For each mode, the total synchrotron radiation power is listed as well as the surface power density normal to the beam at the first absorber masks which are located 6.5 m from the midpoint of the wiggler magnet. These power intensities are for the anticipated magnetic field profile (slightly squarer than sinusoid) and are a few percent greater than would be obtained using equations (1) through (5d). These peak normal power densities for Beam Line VI are more than a factor 10 greater than previously encountered for beam lines at SSRL.

The vertical and horizontal opening angles are given in Table I. The vertical and horizontal spatial distribution of photon intensities is shown in Figure 2. The horizontal opening angle $\Theta_h$ of the Beam Line VI Mode E beam is 11.5 times greater than the characteristic vertical opening angle $\Theta_v$.

TABLE I

Some Operating Modes and Corresponding Synchrotron Radiation Power Intensities For LBL/Exxon/SSRL Beam Line VI

| Mode | | A | C | E |
|---|---|---|---|---|
| Electron Energy, E | [GeV] | 3.0 | 3.0 | 3.7 |
| Electron Current, I | [A] | 0.1 | 0.2 | 0.1 |
| Wiggler Magnetic Field, B | [T] | 1.30 | 1.75 | 1.75 |
| Total Synchrotron Radiation Power, P | [kW] | 1.89 | 6.85 | 5.21 |
| Horizontal Opening Angle, $\Theta_h = K/\gamma$ | [mrad] | 1.45 | 1.95 | 1.58 |
| Vertical Opening Angle, $\Theta_v = 1/\gamma$ | [mrad] | 0.170 | 0.170 | 0.138 |

For First Masks At z = 6.5 m from source:

| | | | | |
|---|---|---|---|---|
| Photon Beam width, $2\Theta_h z$ | [mm] | 18.8 | 25.3 | 20.5 |
| Photon Beam heighth, $2\Theta_v z$ | [mm] | 2.21 | 2.21 | 1.79 |
| Peak Normal Surface Power Density, W" | [kW/cm$^2$] | 7.59 | 20.5 | 23.3 |

Note: Mode A is anticipated typical operation for first year while Modes C and E represent later upgraded performance.

To grasp the significance of these power densities, it is illustrative to compare them to well known power sources. Some power densities for black body thermal radiation are shown in Figure 3. The power density at the surface of the sun and at the surface of a typical tungsten filament are shown for reference. Also shown are the power densities anticipated for Beam Line VI Modes C and E, both for normal impingement and for striking a 1/20 slope. As can be seen, the normal impingement power density significantly exceeds that at the sun's surface and the 1/20 impingement exceeds that from a tungsten filament. These numbers have the physical significance that if the Beam Line VI power densities impinged on a surface of zero thermal conductivity then the surface temperature would rise to the temperatures indicated (neglecting melting and vaporization). The heat transfer rates associated with conventional arc welding are of the order of $10^4$ W/cm$^2$ which indicates that the Beam Line VI components are being asked to survive against the power intensities of a welding torch. As suggested in the cartoon of Figure 4, the photon beam might be thought of as a disintegrator.

3. Steady Heat Transfer to Water Tubes

For a water cooled object with no heat input, the entire object will stabilize at a temperature corresponding to that of the inlet water. If the object is next subjected to a steady rate of surface heat input, the temperature of the impinged surface of the mask will rise and then stabilize at an elevated temperature. The amount of this temperature excursion is dependent on the configuration of the object and its cooling circuits and is the sum of the temperature differences associated with conduction, film heat transfer and bulk water temperature rise.

The temperature difference due to conduction can be calculated by the familiar equation for heat transfer by thermal conduction[6]

$$\frac{P}{A} = -k \frac{dT}{dx} \tag{6}$$

for one-dimensional flow where P/A is heat flux per unit area, k is thermal conductivity and dT/dx is the temperature gradient. For three dimensional steady heat flow with constant k, the differential equation becomes

$$\nabla^2 T + \frac{q'''}{k} = 0 \tag{6a}$$

where $q'''$ is heat input to a unit volume. From these a temperature difference $\Theta_k$ between front surface and coolant passage wall can be calculated.

After the heat has been conducted to the cooling tube wall, it then must be transmitted through the boundary layer into the bulk of the water flow. Water flow for such circuits is commonly turbulent as this gives enhanced heat transfer. Several equations have been proposed for the heat transfer through the boundary film[7] and a suitable one appears to be that due to Sieder and Tate[8]

$$\frac{PD}{A\Theta_f k_b} = 0.027\left(\frac{DV\rho}{\mu}\right)_b^{0.8} \left(\frac{c_p\mu}{k}\right)_b^{1/3} \left(\frac{\mu_w}{\mu_b}\right)^{-0.14} \tag{7}$$

where P/A is heat flow per unit area of surface, $\Theta_f = T_w - T_b$, D is diameter of coolant passage, V is velocity, $\rho$ is coolant density, $\mu$ is coolant viscosity, $c_p$ is specific heat and subscript w indicates evaluation at wall temperature while subscript b indicates evaluation at bulk coolant temperature. The groups in parenthesis are dimensionless. For water, this can be expressed in practical units as

$$\frac{P}{A} = C_{st}\, \Theta_f\, V^{0.8}\, D^{-0.2}\, (\mu_w/\mu_b)^{-0.14} \tag{7a}$$

where P/A is power per unit area [watts/mm$^2$], $\Theta_f$ in°C, $C_{st}$ = constant dependant on temperature which equals 0.0067 at 10°C and equals 0.0098 at 40°C, V is flow velocity [m/sec], D is passage diameter [mm] or the hydraulic equivalent (4 x area/perimeter) for non-circular passages.

As the coolant moves through its passage, it will pick up heat along the way and its bulk temperature will increase as

$$\Theta_b = \frac{P_b}{c_p \rho Q} \tag{8}$$

where $\Theta_b$ is coolant bulk temperature rise to point in circuit being considered, $P_b$ is power input to coolant over same length of coolant circuit, $c_p$ is specific heat, $\rho$ is density, Q is coolant volumetric flow rate. For water, this becomes

$$\Theta_b\ [°C] = 2.40 \times 10^{-7} \frac{P_b\ [W]}{Q\ [m^3/s]} \tag{8a}$$

or

$$\Theta_b\ [°C] = 0.0038 \frac{P_b\ [W]}{G\ [\text{U.S. Gallons/min}]} \tag{8b}$$

One needs to evaluate the sum of $\Theta_k + \Theta_f + \Theta_b$ for several front surface locations to determine the location of maximum temperature.

4. Thermal Stress Fatigue

When metals are subjected to repetitive cycling of stress (or strain), fatigue cracking and ultimate failure can occur at stress levels below the yield stress of the parent material. Fatigue failure data is commonly plotted on an S-N diagram such as that shown in Figure 5 for oxygen free copper subjected to alternating tension and compression.

If an unrestrained object undergoes a temperature rise $\Theta$ each element of the object will undergo a strain change of

$$\varepsilon_x = \alpha \Theta \tag{9}$$

where $\alpha$ is thermal coefficient of expansion

If instead the object is free to expand in two dimensions but is restrained in the third dimension (perhaps the longest dimension) then there will be no strain in that third dimension but there will be a corresponding thermal stress of

$$\sigma_t = \varepsilon_t E = \alpha E \Theta \tag{10}$$

where E is Young's modulus of elasticity.

If the object is restrained in two dimensions and free to expand in the third dimension, then the thermal stresses are given by

$$\sigma_t = \frac{\alpha E \Theta}{1 - \upsilon} \tag{11}$$

where $\upsilon$ = Poisson's ratio. This equation would apply for surface heating of a plate where the material is free to expand normal to the plate surface but is fully restrained in the two lateral directions. Poisson's ratio for copper is approximately 0.35 so two directional restraint can produce thermal stresses more than 50% greater than for one directional restraint. Full restraint is seldom achieved in practice so thermal stresses are less than indicated by these equations. More extensive calculations, such as by 3D finite element computations, can be used to calculate actual stresses associated with the actual temperature distributions.

## 5. Absorber Masks for LBL/Exxon/SSRL Beam Line VI

Masks are located along beam lines to absorb synchrotron radiation photon power not transmitted through to the experiment. Several of the masks on Beam Line VI are subjected to intense power levels and are discussed here.

## 5.1 First Masks

The movable mask on Beam Line VI can be inserted so as to intercept and fully stop all synchrotron radiation power from passing further down the beam line. The configuration chosen for this movable mask has two elements in "V" arrangement as shown in Figure 6. Each element has a horizontal slope of 1/17.5 ($\alpha$ = 3.28°). Space considerations prevented use of a longer mask with a more gradual slope. When a wiggler photon beam strikes a horizontally sloped surface, it produces a trace on the mask surface which is very long and of small height as illustrated in Figure 7. For the Beam Line VI movable mask this works out to be an aspect ratio on the surface of approximately 200:1.

The movable mask is located $\sim$ 6.5 m from mid-length of the wiggler source. The greatest surface temperature rise occurs for Mode C which produces a peak surface power density on the 1/17.5 sloped mask of 1170 W/cm$^2$ and a lineal power density of 200 W/cm.

The thermal flow pattern resulting from this heat input is shown in Figure 8. Heat transfer in the lengthwise direction of the mask is neglected. The heat input has a vertical bell-shape distribution as was shown in Figure 2 and is depicted here by the arrows going into the surface with an equal quantity of heat flow between adjacent arrows. The heat flow from the surface to the water passages is parallel to the flux lines shown while the orthogonal lines are isotherms. The thermal flow pattern shown here was drawn by hand after several iterations so as to simultaneously satisfy conduction equation 6 and film heat transfer equation 7.

It is interesting to note the approximately semi-circular shape of many of the isotherm lines. This suggests that one might get a good approximation for this heat transfer by considering heat flow through a thick cylindrical wall of 180° angular extent.

The case of a hollow cylinder has been considered by Carslaw and Jaeger[9] and, after adjustment to a hollow half-cylinder, the solution is

$$T_c - T_d = \frac{W'}{\pi} \ln\left(\frac{d}{c}\right) \qquad (12)$$

where c and d are the inner and outer radii respectively and W' is the lineal power density such as from equation 5c. It would seem logical to select the inner radius equal to W'/W". However, better agreement with the results of the thermal flow plot of Figure 8 is obtained if the inner radius c is reduced slightly to

$$c[\text{mm}] = 0.75 \frac{W' \ [W/\text{mm}]}{W'' \ [W/\text{mm}^2]} \qquad (12)$$

where W" is the peak surface power density such as from equation 5d. The outer radius d can be taken at a mean distance to the water passages and the resulting calculated temperature difference is not very sensitive to the value selected for d.

For the above-described thermal flow and with a water velocity of 9.1 m/s (30 feet/sec), the conduction, film and bulk temperature rises ( $\Theta_k$, $\Theta_f$ and $\Theta_b$ respectively) were calculated [10] for the movable mask and are plotted in Figure 9 for 10°C inlet water temperature (higher inlet water temperature increases the water viscosity and results in smaller thermal excursions). The peak temperature rise is 92-10 = 82°c. If the mask were fully restrained in two lateral dimensions, this would result in a thermal stress range (equation 11) of 253 MPa (36700 psi) with the thermal stress amplitude being half as much. An estimate of the actual restraint reduces the thermal stress amplitude to $\pm$ 82 MPa (11,900 psi). An upper estimate of the number of thermal cycles to be encountered is (40/day)(250 days/year)(10 years) = $10^5$ cycles and the corresponding fatigue failure stress is $\pm$125 MPa (18000psi) which appears amply safe.

The semi-circular water passages were chosen somewhat arbitrarily.

A water passage of greater depth (perpendicular to the impinged surface) would enhance heat transfer slightly but at the expense of greater volumetric coolant flow and/or lower coolant velocity. There is room for further optimization.

What is the optimum distance from the front surface to the coolant passages? As this distance is decreased, the conductive temperature drop becomes less. But on the other hand, as the distance is increased the effective film heat transfer area to water becomes greater thereby reducing the film temperature drop. The 3.2 mm dimension adopted for the movable mask gave a lower total temperature drop than for a 1.2 mm distance that was also considered. Subsequent calculations have indicated that a dimension of $\sim$10 mm would have been slightly better yet.

During the design, a configuration with vertically sloping mask surfaces at a slope of 1/35 ($\beta$ = 1.64°) was considered[11]. When the wiggler photon beam strikes a vertically sloped surface, it produces an impinged area that has an aspect ratio close to unity as shown in Figure 10. In this case, one gains little benefit from lateral and longitudinal heat transfer and one gets a thermal flow pattern similar to that of Figure 11 for uniform surface heating. In this case, it is desirable to make the distance from the front surface to the water cooling tubes as small as possible. Even with this distance reduced to 1.3 mm and with the 1/35 slope, this arrangement had a greater total temperature rise than for the 1/17.5 horizontally sloped surfaces. Thus, the horizontally sloped design was the one implemented.

The first fixed mask is located directly upstream from the movable mask. It has a vertical clear aperture of 20 mm and a horizontal clear aperture of 39.6 mm at the exit and 83.2 mm at the entrance. Under certain infrequent operating conditions, the SPEAR beam can impinge on the side

walls but not the floor or ceiling of this fixed mask. The side walls are of a construction similar to that for the movable mask but are at a slope of 1/35 ( $\alpha$ = 1.64°) so that the total temperature rise on the surface is approximately one half that for the movable mask and the thermal stresses are also correspondingly lower[12].

5.2 Vertical and Horizontal Slits

The vertical slit assembly is located approximately 11.5 m from the midpoint of the wiggler magnet. The vertical slit assembly consists of two intensely water cooled copper absorbing masks with one located above the beam centerline and the other located below. These masks are hinged at their upstream end and can be moved into the synchrotron radiation beam by means of a positioning system located outside of the vacuum and operating through bellows. The vertical aperture is approximately 50 mm at the entrance and is 11.6 mm at the exit when fully opened.

The downstream end of each mask can move from its open position 5.8 mm outboard of centerline to 3 mm beyond centerline or until it closes against the other mask, whichever occurs first. The two masks are interlocked externally so as to prevent damage when the blades fully close.

The steepest impingement of the photon beam onto the vertical slit is at a slope of 1/16 ($\beta$ = 3.6°) and this occurs when one of the masks is 3 mm beyond centerline. This results in a peak surface power density of approximately 480 watts/cm$^2$. Each mask is a brazed copper assembly similar to that of one arm of the movable mask shown in Figure 6 but with 22 semicircular water passages in each mask and a surface to coolant passage distance of 3.0 mm. With a water velocity of 9.1 m/s (30 ft/sec), a peak front surface temperature rise of 71°C was calculated taking into account that a total of 30% of the heat is transmitted laterally and longitudinally. If the mask were fully restrained in two dimensions, a

thermal stress amplitude of ± 110 MPa (16,000 psi) would result. However, the mask is not fully restrained in two dimensions so a final calculated thermal stress amplitude of ± 63 MPa (9,100 psi) is calculated. This mask will receive less than $10^5$ cycles of heating so the indicated cyclic stress levels appear adequately safe.

The horizontal slit assembly is located approximately 12.0 m from the midpoint of the wiggler source. Its construction is similar to that of the vertical slit assembly with two separate masks hinged at the upstream ends. This assembly has a horizontal aperture of ∿100 mm at the entrance and 56 mm at the exit when fully opened. The downstream end of each mask element can move across the full 56 mm aperture unless it contacts the opposite element sooner. Thus, a slot of any chosen width may be placed anywhere within the 56 mm available aperture. The steepest impingement on the horizontal slit mask element is 1/7.0 ( $\alpha = 8.1°$). This corresponds to a peak surface power density of 900 W/cm$^2$. The horizontal slit masks also are of copper construction similar to that shown for the movable mask in Figure 6 and with a thermal flow pattern similar to that of Figure 8. Each mask element has eight semicircular flow passages located 3.0 mm from the front surface. With water velocity of 7.3 m/s (24 ft/sec), the maximum total temperature rise to the front surface of the mask is 83 degrees C. If fully restrained in two lateral dimensions, the corresponding thermal stress amplitude would be ± 128 MPa (18,600 psi). However, estimates of the actual restraint reduce this to ± 73 MPa (10,600 psi). The number of heating cycles should be well below $10^5$, so these cyclic stress values seem amply safe.

5.3 Downstream Masks

Typically, more than 60 percent of the synchrotron radiation power is absorbed in the graphite filter and on the focus mirror. Less than 40

percent is transmitted downstream towards the beryllium window. The focus mirror deflects the photon beam at an angle variable from 0.42 degrees to 1.00 degrees. Misadjustment of the mirror or missteering of the SPEAR beam may cause a significant fraction of the photon beam to miss the mirror.

The pivot mask is designed to accept this stray radiation. The floor and two side walls of this mask require water cooling for beam power densities that are about one third of those encountered on the upstream masks previously described. If the cooling passage arrangement for the previously described masks were to be used for the pivot mask, an array of 72 semicircular water passages would have been required. A simpler arrangement was sought which lead to the configuration shown in Figure 12. Commercially available[13] phosphorus deoxidized copper tubing with spiral internal fins will be brazed to the outside of the heavy copper walls of the mask. Lips on the walls will be rolled over to retain the finned tubing in position during brazing. These rolled lips will also provide enhanced heat transfer capability to the portions of the tube most remote from the impinged surface. Calculations indicate that this arrangement is satisfactory for the somewhat lower power densities encountered here.

The beryllium window mask is designed to absorb synchrotron radiation which otherwise would miss the foil portion of the beryllium window and would hit the window frame. The exit aperture of this mask is 3 mm high by 18 mm wide. The configuration and cooling of this mask will be similar to that for the pivot mask just described.

The monochromator beam dump will consist of an upper mask located upstream of the monochromator and a lower mask located downstream of the monochromator as shown diagrammatically in Figure 13. Only monochromatized synchrotron radiation can pass through this arrangement. Even if a monochromator crystal fails, no straight-through rays can pass through this

arrangement. The thermal and mechanical designs of this monochromator beam dump are yet to be finalized.

6. Transient Surface Temperature Rise of Fast Valve

Beam Line VI contains a CERN-type fast valve located approximately 7.8 m from the wiggler midpoint. This valve will close in ∿10 ms after being triggered by a vacuum fault. It was of interest to know the rate of temperature rise of the titanium alloy valve plate upon closure in order to know how quickly the SPEAR beam would have to be turned off. For Mode E operation, the peak normal-impingment power density at this location is 16.1 $kW/cm^2$ with a horizontal to vertical aspect ratio of 11.5. A good approximation for this case can be obtained by assuming an infinite aspect ratio and assuming that the horizontal lineal power density is uniformly distributed on a half cylinder recess in a semi-infinite block and assuming a cylindrical radius such that both the surface power density and lineal power density match the respective peak values for Mode E operation. The temperature rise for this case can be calculated using the formulas given by Carslaw and Jaeger [14] for heating of a cylindrical hole in an infinite medium. The resulting temperature rise is shown in Figure 14 for the titanium alloy plate as well as for aluminum and copper if such were used. At early times, the +0.5 power slope corresponds to that for uniform surface heating of a semi-infinite slab. At later times the slope becomes lower due to heat conduction in the vertical direction as well as the depth direction once the heated zone has reached a depth comparable to the radius of the cylinder. The results indicate that the titanium alloy surface would start to melt within a few milliseconds. After consultation with SSRL staff, it was decided that the most prudent course was to abort the SPEAR beam by turning off the R-F power simultaneous with initiation of

fast valve closure, thereby turning off the SPEAR beam before the valve plate can move into the synchrotron radiation beam.

7. Heating of Beam Line VI Mirrors and Crystals

For Beam Line VI, the focus mirror is located approximately 12.8 m from the wiggler midpoint. The incidence angle on this mirror initially will be 0.21 degrees and may increase in the future to 0.50 degrees. The mirror is mounted to a mirror-bending mechanism and is cooled by thermal radiation to the surroundings. It is anticipated [15] that the mirror temperature will rise > 100°C and that the mirror may require focus adjustment after temperature excursions. At the upstream end of the mirror, there is a water cooled mask with an incidence angle of approximately 3°. It is cooled by five parallel stainless steel water tubes brazed into slots in the rear surface of this copper mask[15].

The crystals in the monochromator can be subjected to significant heating. The focussed image of the wiggler source occurs closely downstream of the monochromator. The incidence angle onto the monochromator crystals can vary from small angles to more than 60°. Approximately one third of the synchrotron radiation power remains after passage through the focus mirror, beryllium window and graphite filters. This is concentrated onto an area of the first crystal that is comparable in size to the electron beam size at the wiggler source. Preliminary calculations[16, 17] indicate that temperature rises of many hundreds of degrees celsius can be anticipated.

One hypothetical crystal configuration used for early analysis of crystal heating is shown in Figure 15 with the heat confined to a zone on the top surface and with the two side walls (y = 0 and y = b) held at a fixed temperature $T_o$. For a hypothetical heat input, the temperature

profiles for the front surface of the crystal are shown in Figure 16. There clearly will be large variations in the crystal d-spacing associated with such large variations in the surface temperature. For this same hypothetical case, the mechanical stresses and strains associated with these temperature excursions were calculated and are displayed graphically in Figure 17. Both the change in d-spacing and the distortion of the crystal surface may significantly effect the research performance of the monochromator. These considerations, possible crystal fracture and possible enhanced cooling means need considerable further study.

## 8. Looking To The Future

It appears that many wiggler/undulator beam lines will be built in the coming years. A Beam Line IX for SSRL is being contemplated by LBL/Exxon/SSRL. SSRL is planning a high power undulator line for PEP. NSLS/BNL is designing a superconducting wiggler beam line[18] with power densities approaching those of Beam Line VI. LBL has proposed construction of the Advanced Light Source which ultimately would have 12 wiggler/undulator beam lines plus their associated branch lines. SSRL is considering a two-ring facility[19] which could ultimately accommodate more than 50 wiggler/undulator beam lines. Many of these will have power densities at least comparable to those described here for Beam Line VI. The earlier equations indicate that total synchrotron radiation power varies as $E^2$ and that synchrotron radiation power density per unit solid angle varies as $E^4$. Thus, thermal and materials problems could be even more significant for some of the proposed beam lines. Table II indicates significantly greater synchrotron radiation power intensities if the Beam Line VI wiggler were installed in a 5-6 GeV, 0.1A electron ring with the corresponding SPEAR 3.7 GeV values included for comparison.

TABLE II

Comparisons of Calculated Power Intensities If Beam Line VI Wiggler Operated at 5-6 GeV.

| | | SPEAR Mode E | New Ring | |
|---|---|---|---|---|
| Electron Energy, E | [GeV] | 3.7 | 5.0 | 6.0 |
| Electron Current, I | [A] | 0.1 | 0.1 | 0.1 |
| Wiggler Magnetic Field, B | [T] | 1.75 | 1.75 | 1.75 |
| Total Synchrotron Radiation Power, P | [kW] | 5.21 | 9.5 | 13.7 |
| Horizontal Opening Angle, $\Theta_h \simeq K/\delta$ | [mrad] | 1.58 | 1.17 | 0.97 |
| Vertical Opening Angle, $\Theta_v \quad 1/\delta$ | [mrad] | 0.138 | 0.102 | 0.085 |
| At z = 6.5 m from Source | | | | |
| Photon Beam Width, $2\Theta_h.z$ | [mm] | 20.5 | 15.2 | 12.7 |
| Photon Beam Heighth, $2\Theta_v.z$ | [mm] | 1.79 | 1.33 | 1.11 |
| Peak Normal Surface Power Density, W" | [kW/cm$^2$] | 23.3 | 78. | 161. |

Beam Line VI has done quite a bit of pioneering effort for high power beam lines. With the advent of so many future high power beam lines, it is appropriate to consider ways in which things can be done even better in the future.

8.1 Better Analytical Tools

The synchrotron radiation power density onto a specific surface along a beam line is dependent upon a large number of parameters associated with the design and operation of the electron storage ring and of the beam line. A computer program to calculate such synchrotron radiation power densities is now being developed at LBL by E. Close and others. This program will take into account the following parameters:

Electron beam energy and current (E, I),

Electron beam spot size, ($\sigma_x, \sigma_y$),

Electron beam angular divergence ($\sigma_{x'}, \sigma_{y'}$),

Electron beam orbit deviations ($\Delta x, \Delta y, \Delta x', \Delta y'$),

Wiggler/undulator length, period and magnetic field ($L, \lambda, B$),

Angular distribution of photon intensity and energy,

Reflection/absorption at intermediate impinged surfaces.

Defining apertures,

Focussing by mirrors.

One will be able to input values or ranges for the above parameters and let the computer calculate the corresponding power densities at selected points on the beam line. For Beam Line VI, such calculations were done by hand on a conservative basis, perhaps overly conservative. This new program will give us a much more rational basis for the thermal design of beam line components.

Three dimensional computer programs to calculate temperature distributions and the resulting thermo-mechanical stresses and strains have

been available for some years. However, most of these are not user-friendly and typically require months to achieve proficiency at their use. User-friendly versions, particularly ones suitable for engineering computer work stations, are being sought.

8.2 Better Mask Configurations

Further study and analysis should yield better mask configurations. Other cooling passage arrangements may result in better heat transfer and reduced surface temperatures. The brazed configuration now used are expensive so less costly arrangements are desired.

Compared to annealed oxygen free copper, other materials may have enhanced thermal fatigue characteristics coupled with adequate thermal conductivity and ultrahigh vacuum compatability. Several dispersion-strengthened copper alloys[20] appear to offer significantly better fatigue properties with only a slight loss of thermal conductivity but their ultrahigh vacuum compatability needs to be verified. Another possibility is electro-deposited copper which initial studies indicate has significantly enhanced mechanical properties with comparable thermal conductivity and ultrahigh vacuum compatability but its resistance to being annealed by bake out or other elevated temperture operations is yet to be evaluated.

8.3 Crystal/Mirror Heating

As discussed earlier, the heating of crystals and mirrors has yet to be fully addressed on high power beam lines. What temperature can these mirrors and crystals stand? What are the outgassing characteristics of these materials at elevated temperatures? What are the effects of d-spacing variations and surface distortion to the experimenter? What temperature distributions might cause fracture? Will elevated temperatures cause degradation of multilayer crystal surfaces due to diffusion? Can

coolant channels be incorporated directly into the crystals and mirrors? Will turbulent flow in the coolant channels cause noise that would degrade optical performance? It has been suggested[17] that laminar flow of liquid metal coolants may offer advantages. Much remains to be studied.

8.4 Reduction of Incident Power Densities

There are several ways to reduce the power density onto beam line surfaces but these often involve compromises to the design goals of the beam line. The angle of incidence can be reduced but this lengthens components which in turn increases the cost and overall length of the beam line. As the incidence angle is reduced, reflection of the lower energy photons needs to be considered along with variation of the incidence angle due to machining tolerances, surface finish, thermal distortion, etc. One can locate components further from the source (or from the image) where power densities are lower. If one is interested primarily in the higher energy portion of the photon spectrum, filters of graphite (for example) can be imposed to absorb the lower energy portion. Conversely, if one is not interested in the higher energy portion of the photon spectrum, one can introduce one or more low incidence mirrors to absorb the higher energy photons. Finally, for those experiments in which spectral brilliance is of importance, the use of undulator magnets may offer advantages over wiggler magnets.

9. Conclusions

The power intensities on wiggler beam lines, such as LBL/Exxon/SSRL Beam Line VI, are formidable. Solutions adequate for the purpose have been found for the Beam Line VI masks. Thermal considerations for the Beam Line VI monochromator crystals have been only partially addressed.

It appears there will be many wiggler/undulator beam lines in the future. There is a need for better user-friendly analytical tools to provide faster more accurate answers regarding power densities, temperatures, stresses and strains. More effective and less costly mask configurations should be sought. The thermal impact on gratings, crystals and mirrors needs further study as does the impact of these parameters on the experiment itself. Finally, the dialogue that now exists between the various groups designing high power beam lines should continue and be strengthened for the joint benefit of all.

## 10. Acknowledgements

I wish to acknowledge the many individuals at Lawrence Berkeley Laboratory and elsewhere who have contributed to the material presented herein. In particular, I wish to acknowledge E. H. Hoyer, D. B. Hunt and K. J. Kim of LBL for their many helpful discussions on these topics and to thank the Beam Line VI Team for their follow-through in the design and fabrication of these components.

## References


1. Hoyer, E., "A New Wiggler Beam Line for SSRL", Nucl. Instr. & Methods, 208, (1983), p. 117.

2. D.M. Mills, D.H. Bilderback and B.W. Batterman; "Thermal Design of Synchrotron Radiation Exit Ports at CESR." IEEE Trans. Nucl. Sci. Vol. NS-26, No. 3, p. 3854 (June 1979).

3. C. Jako, N. Hower and T. Simon; "Installation and Thermal Design of Synchrotron Radiation Beam Ports at SPEAR." IEEE Trans. Nucl. Sci., Vol. NS-26, No. 3, p. 3851 (June 1979).

4. G. Brown, K. Halbach, J. Harris and H. Winick, "Wiggler and Undulator Magnets - A Review." Nucl. Instr. & Meth., 208 (1983) p. 65-77.

5. K. J. Kim, private communication.

6. W.H. McAdams, "Heat Transmission." 3rd edition, McGraw-Hill (1954).

7. R. T. Avery, "Film Heat Transfer Equations for Turbulent Water Flow." LBL Note LBID-603, 1982.

8. E.N. Sieder and G.E. Tate, Ind. Eng. Chem., 28, 1429-1436 (1936).

9. H.S. Carslaw and J. C. Jaeger; "Conduction of Heat in Solids." 2nd Ed., Oxford Univ. Press 1959, Section 7.2, p. 189.

10. R.T. Avery, "Movable Mask-Design 'H'; Engineering Design." LBL Note LBID-615, 1982.

11. R.T. Avery, "Movable Mask-Design 'V'; Calculations." LBL Note LBID-672, 1982.

12. R.T. Avery, "First Fixed Mask-Engineering Design." LBL Note LBID-604, 1982.

13. Noranda Metal Industries, Inc., Forge-Fin Division, Prospect Drive, Newtown, Connecticutt, 06470, Type SA tubing.

14. H.S. Carslaw and J.C. Jaeger, ibid, Sections 13.5 and 13.6, p. 334 et seq.

15. N. Hower, private communiation.

16. S. Caspi, "Heat Transfer to a Three-Dimensional Solid Prism," LBL Note LBID-725, May 1983.

17. E. Hoyer, "Preliminary Crystal Heat Transfer Calculations," LBL Note LBID-754, June 1983.

18. W. Thomlinson, private communiation.

19. H. Winick et al, "An All Wiggler and Undulator Synchrotron Radiation Source," IEEE Trans. Nucl. Sci., Vol. NS-30, No. 4, p. 3097 (1983)

20. For example: "Glid-Cop" alumina-dispersion-strengthened copper from Glidden Metals Chemical/Metallurgical Division of SCM Corp., 1468 West 9th Street, Cleveland, Ohio 44113; "Cube Alloy" beryllia-dispersion-strengthened copper from Handy & Harman, 850 Third Ave., New York, NY 10022; "DS" electronics-grade zirconia-dispersion-strengthened copper from Raytheon Corp., Microwave and Power Tube Division, 141 Spring, Lexington, Massachusetts 02173

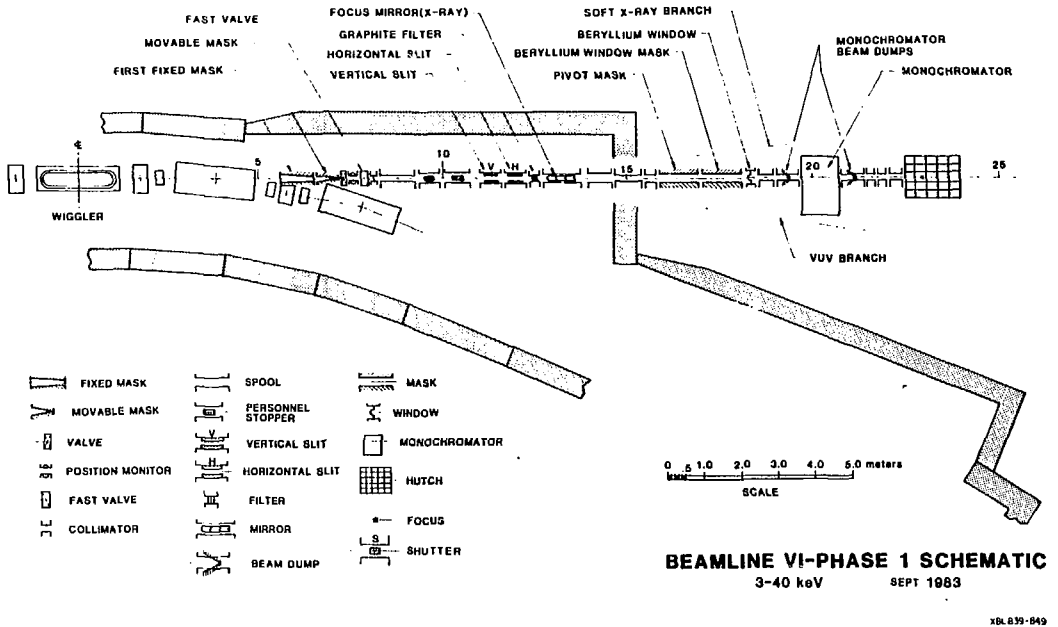


Figure 1. Diagrammatic plan view of LBL/Exxon/SSRL Beam Line VI.

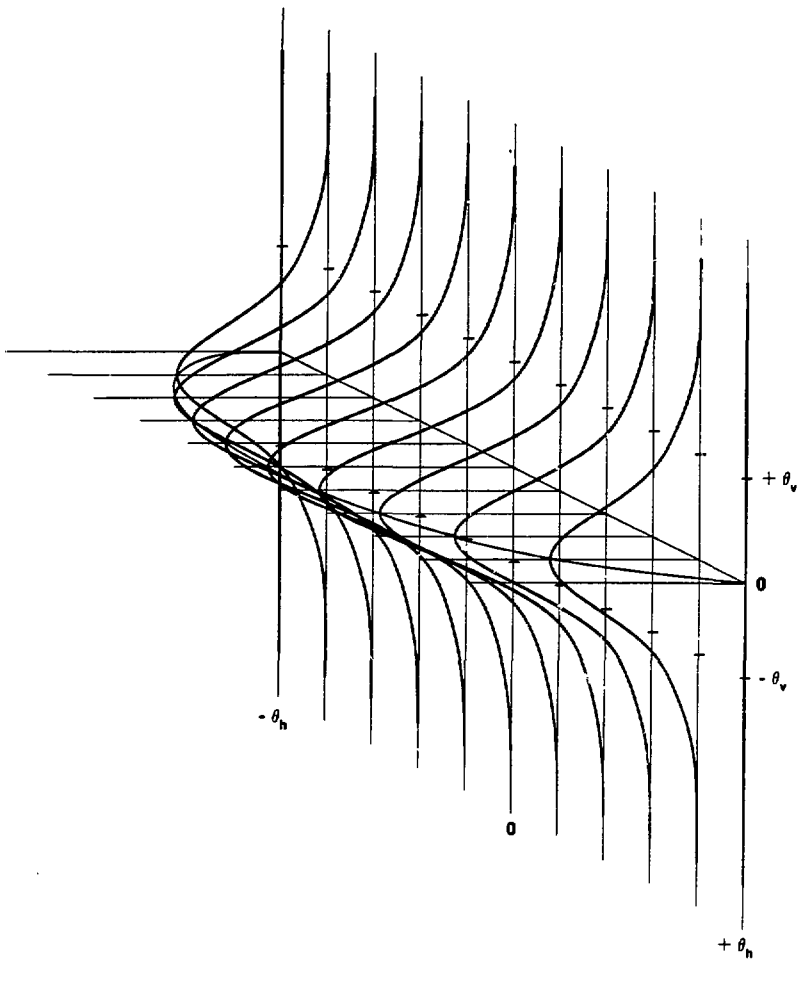


Figure 2. Power density distribution of LBL/Exxon/SSRL Beam Line VI photon beam assuming infinitesimal electron beam size.

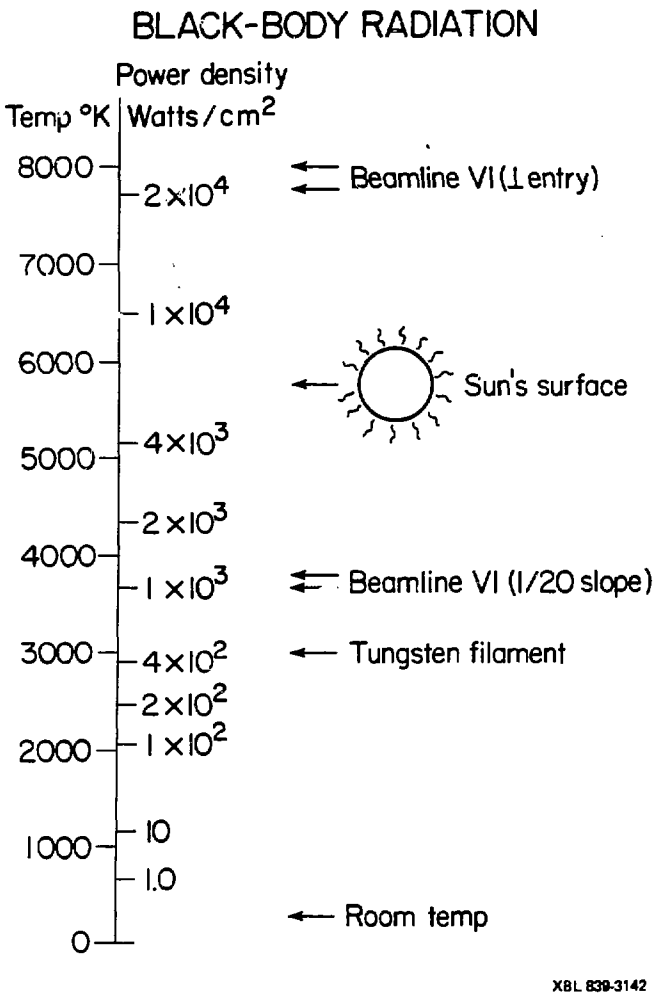


Figure 3. Black-body radiation power densities compared to those expected for the first masks of the LBL/Exxon/SSRL Beam Line VI.

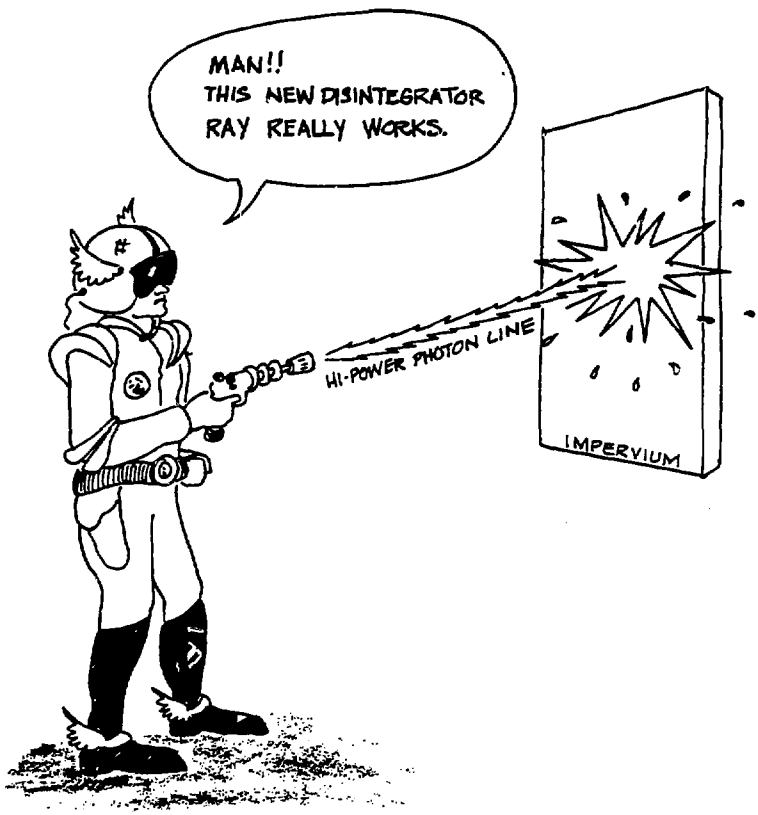


Figure 4. Cartoon depicting intense photon beam.

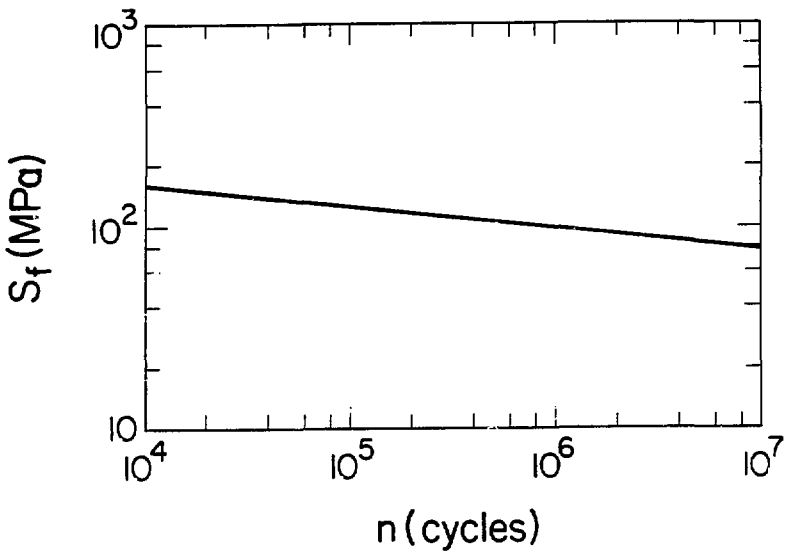


XBL 839-3141

Figure 5. Typical fatigue failure strength of oxygen-free copper subjected to n cycles of alternating tension and compression of amplitude $s_f$.

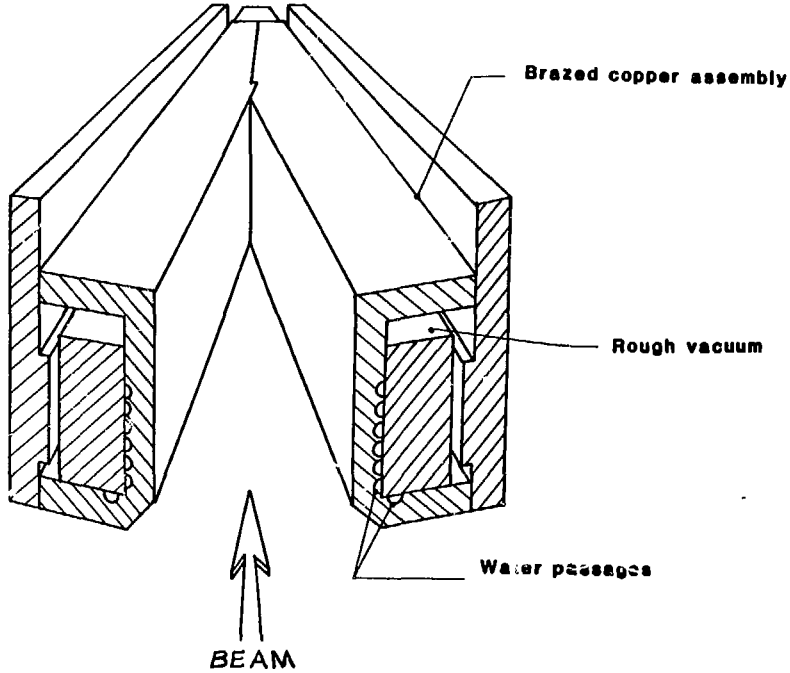


Figure 6. View of the LBL/Exxon/SSRL Beam Line VI movable mask located 6.6 m from source.

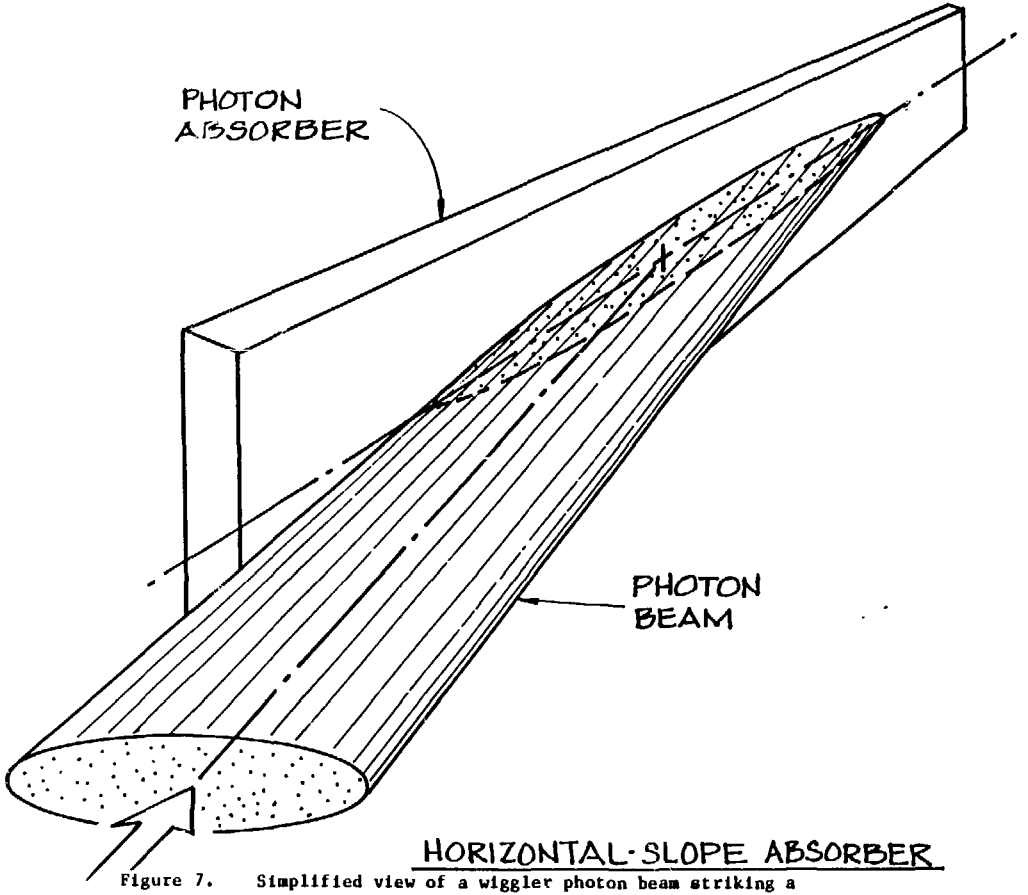


Figure 7. Simplified view of a wiggler photon beam striking a horizontally sloped surface. For example, an 11.5:1 aspect ratio photon beam striking a 1/17.5 horizontal slope results in an aspect ratio of 200:1 on the surface, which approximates narrow line heating.

XBL 839-3135

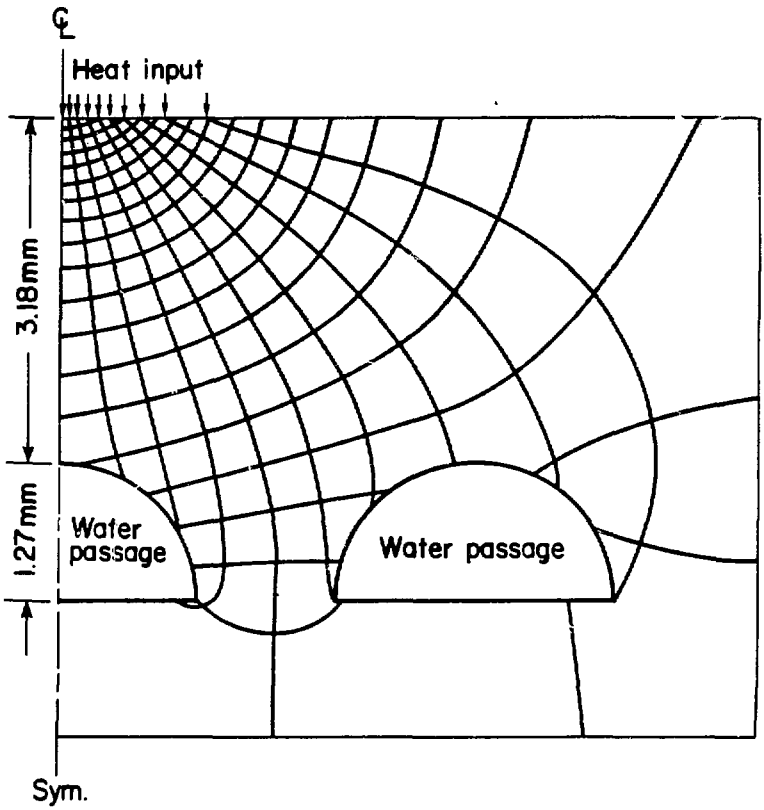


Figure 8. Thermal flow pattern (isotherms and flux lines) within horizontally sloped movable mask for Beam Line VI. Note that a significant amount of heat is conducted vertically to the adjacent water passage. Pattern is symmetrical about centerline.

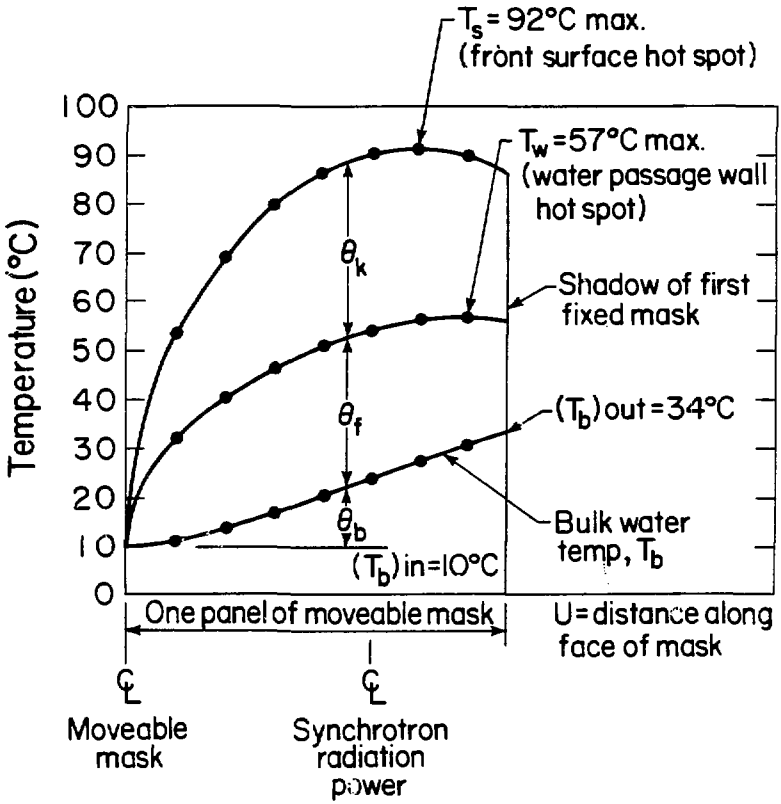


Figure 9. Calculated temperatures for LBL/Exxon/SSRL Beam Line VI photon beam striking one blade of the 1/17.5 horizontally-sloped movable mask (E = 3.0 GeV, i = 0.2A, B = 1.75T)

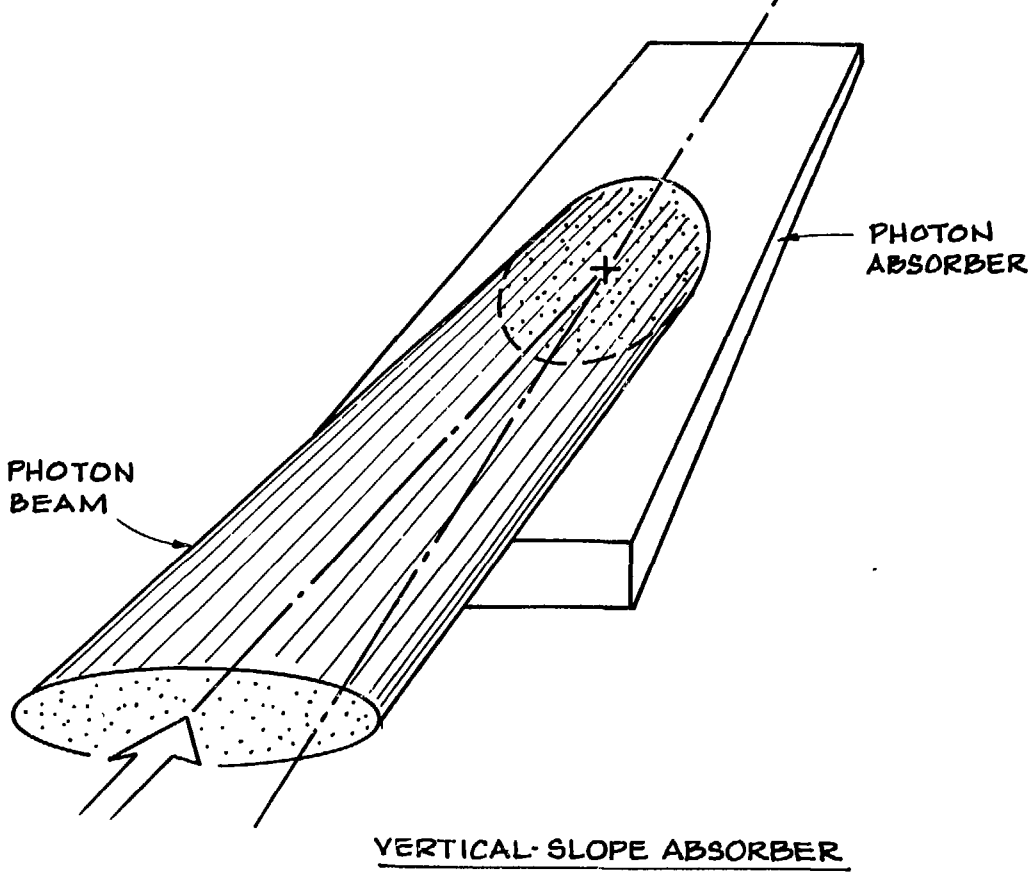


Figure 10. Simplified view of a wiggler photon beam striking a vertically-sloped surface. For example, an 11.5:1 aspect ratio photon beam striking a 1/15.8 vertical slope results in a 0.73 aspect ratio on the surface.

XBL 839-3134

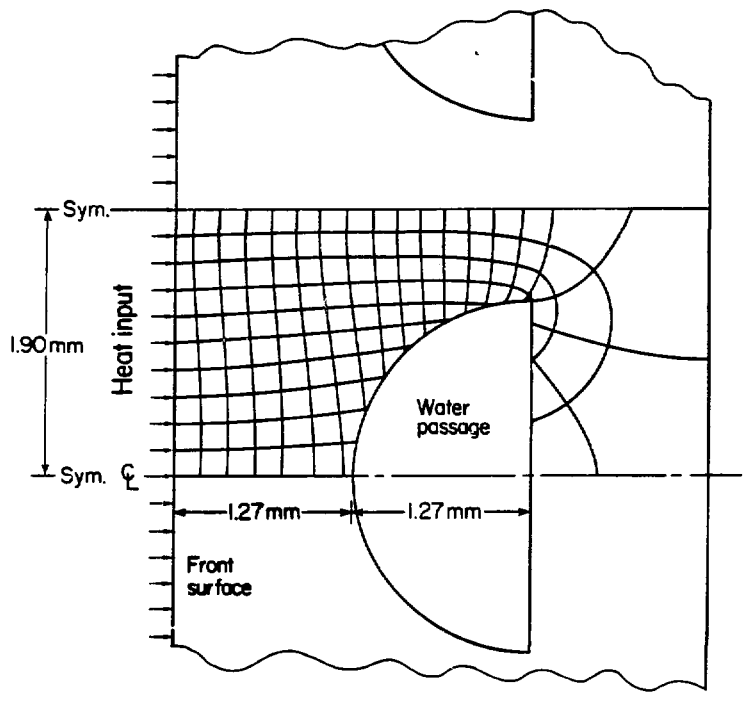


Figure 11. Thermal flow pattern (isotherms and flux lines) for uniform surface heating of a water-cooled mask.

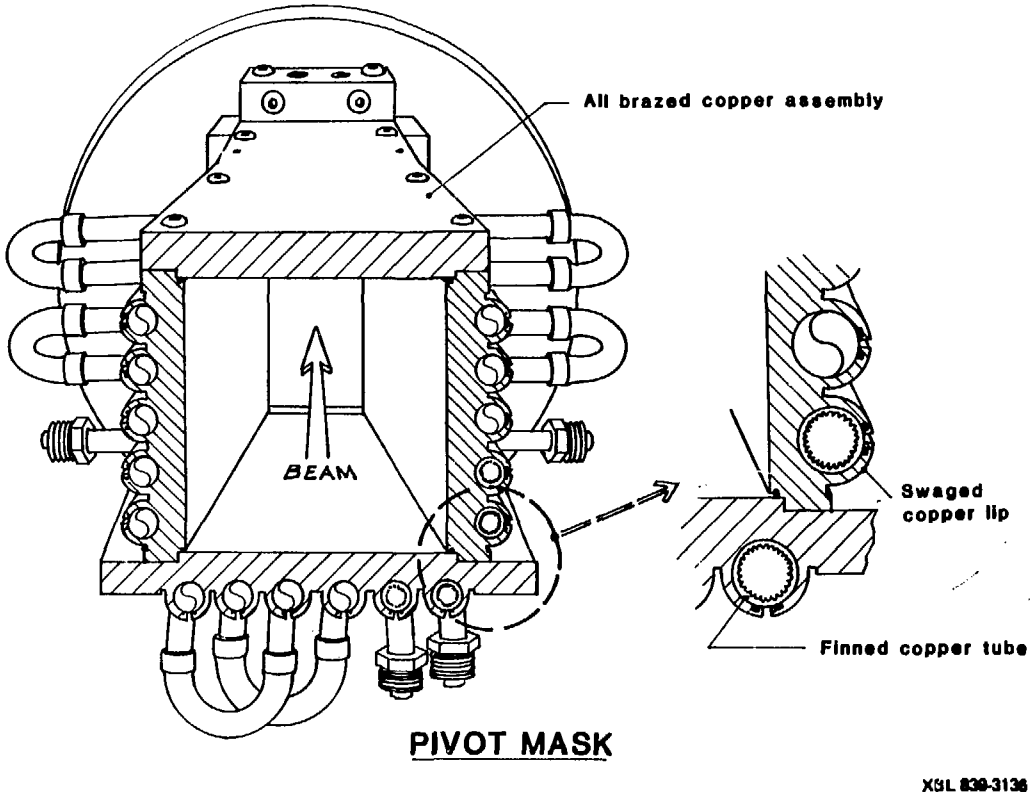


Figure 12. View of the pivot mask for the LBL/Exxon/SSRL Beam Line VI showing use of internally-finned copper tubing to enhance heat transfer at the tube wall.

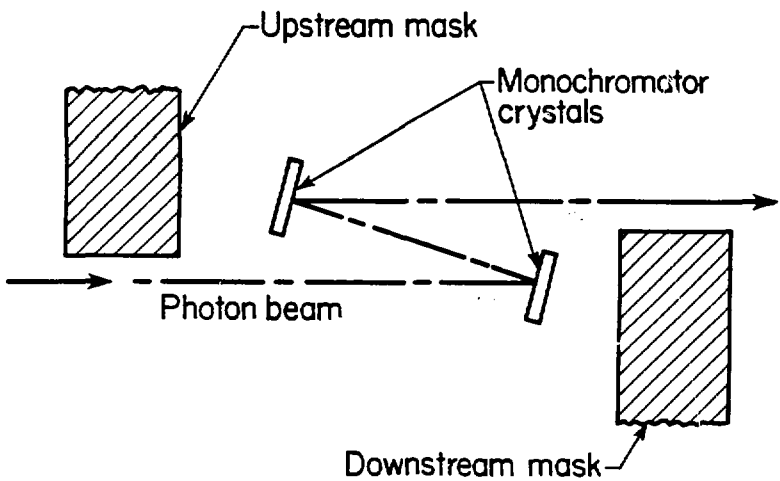


Figure 13. Diagrammatic elevation view of the monochromator beam dump for the LBL/Exxon/SSRL Beam Line VI X-ray line. Only monochromatized light can pass through to the experimenters' hutch.

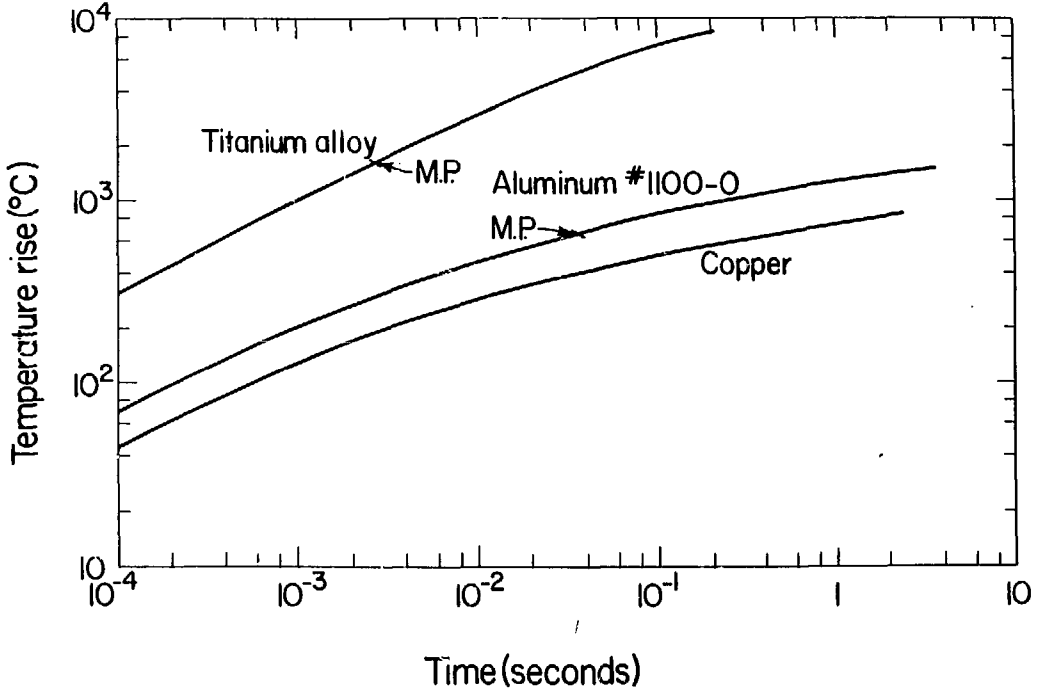


Figure 14. Approximate calculation of peak surface temperature rise versus time for normal impingement of LBL/Exxon/SSRL Beam Line VI photon beam onto fast valve surface at 7.82 m from source. M.P. = melting point. (E = 3.7 Gev, i = 0.1A, B = 1.75T)

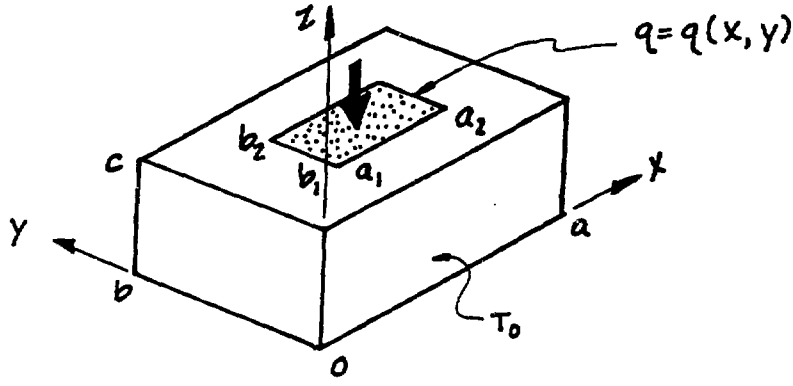


XBL839-852

Figure 15. Configuration assumed for initial analysis of crystal heating with surfaces y = o and y = b held at fixed temperature $T_0$.

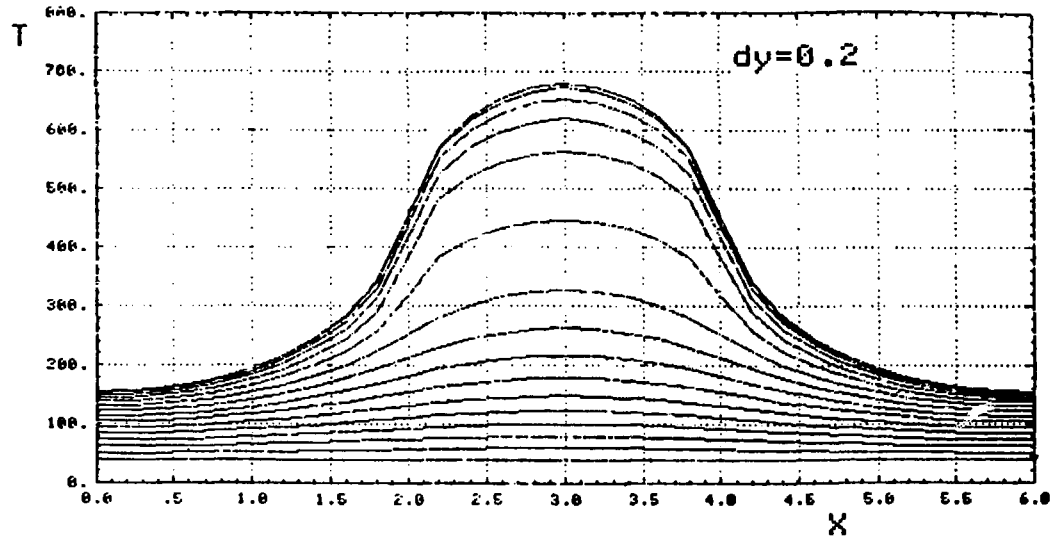


Figure 16. Calculated Front Surface temperature profiles at successive planes based on crystal heating initial analysis.

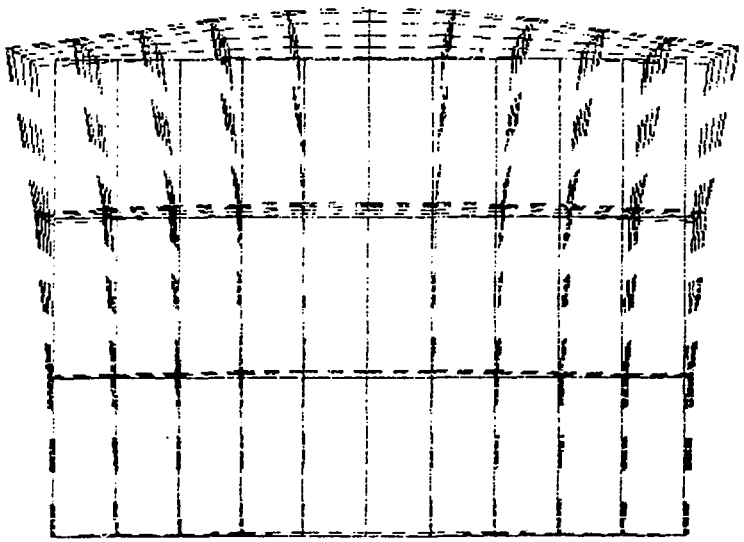

XBL839-851

Figure 17. Crystal deformation (exaggerated scale) depicted by computer initial analysis. Solid lines are without heat input while dashed ones are with heat input.